Stresses in planar normal faulting: shallow compression caused by fault-plane mismatch

Martin H.P. Bott*

Department of Earth Sciences, University of Durham, South Road, Durham DH1 3LE, UK

ABSTRACT

Shallow horizontal compressive stress often occurs near the top of the hangingwall plate in numerical modelling of planar normal faulting, extending horizontally for up to 14 km from the fault plane. This compression is attributed to a potential downward mismatch between the dips of the opposing fault planes which would rotate differentially if unconstrained to remain in contact. The mismatch is suppressed by downward increasing lithostatic pressure which applies equal but opposite couples to the fault planes forcing them to remain in contact. This gives rise to shallow compression and deep tension on both sides of the fault. The potential mismatch originates partly from differential loading on opposite sides of the fault, but also from the anti-symmetrical shapes of the footwall and hangingwall plates. These two contributions oppose each other in normal faulting but reinforce in reverse faulting. The modelling also reveals large fault-parallel compressive stress adjacent to the footwall. This compression acts as a seal inhibiting fluid flow across the fault and preventing upflow adjacent to the footwall. In contrast, smaller fault-parallel tension adjacent to the hangingwall provides a low pressure channel for upward fluid flow adjacent to the fault, giving rise to a zone of weakness. Strain relief in this weak zone, in response to shallow mismatch compression, may explain the so-called normal fault drag near the top of the hangingwall.

© 2008 Elsevier Ltd. All rights reserved.

1. Introduction

Planar normal faulting is the main tectonic process by which the strong upper continental crust is extended. The faulting is associated with seismic activity and occurs in response to horizontal nonlithostatic tension in regions of above average heat flow where the strong and brittle upper crust is underlain by a weak, ductile lower crust (Sibson, 1983, 1989). The tension may arise locally in regions of plateau uplift and rifting from anomalous surface and subsurface loading caused by an upper mantle hot spot or crustal thickening. It may also arise from trench suction/slab pull in continental regions near collision or subduction plate boundaries. The distribution of earthquake foci demonstrates that these faults are approximately planar down to the base of the brittle layer at 6–15 km depth where the earthquakes nucleate and that their dip is between 30° and 60° (Jackson, 1987; Jackson and White, 1989; Yeats et al., 1997). They may terminate at a sub-horizontal detachment surface in the transitional region between the upper

brittle and lower ductile crust. The vertical displacement can be in excess of 5 km.

Planar normal faults formed in earlier active periods are present in many regions, although usually absent from unreactivated Precambrian shields. Examples include the Mesozoic North Sea rifts of Triassic and Jurassic age (Roberts and Yielding, 1991) and the E–W Lower Carboniferous block and trough system of the Northern Pennines, England.

The occurrence of shallow horizontal compression affecting the hangingwall plate in the vicinity of planar normal faults came to my attention from finite-element modelling of normal-faulted half grabens in an elastoplastic upper crust (Bott, 1997). Such shallow horizontal compression is systematically seen in most of these models near the upper surface of the downthrown hangingwall plate within a few kilometres of the fault plane. It is also seen in further unpublished results which include fault friction. The stretching and downbending of the layer can only give rise to horizontal tension at shallow depth in the hangingwall plate. An additional source of shallow compressive stress must therefore be present in planar normal faulting.

An earlier study provides the background for understanding this shallow compressive stress (Bott, 1996). Thin plate flexure theory has usually assumed unconstrained end-loading of a semi-infinite

* Tel.: +44 191 3342284; fax: +44 191 3342301.
  E-mail address: m.h.p.bott@dur.ac.uk

plate to model the flexural deformation of a faulted plate (Gunn, 1943; Watts, 2001, pp. 103–108). When applied to faulting, a discrepancy was found between such results and those of finite-element modelling (Bott, 1996, Figs. 1 and 2). Unconstrained end-loading implies that the surface gradients of each plate differ across the fault because of differential isostatic loading on opposite sides such as footwall basement uplift and hangingwall sediment infill. This must cause a downward widening gap where the plates join along a fault plane. In finite-element modelling, as in reality, the plates are forced to remain in contact preventing such angular mismatch. The suppression of potential angular mismatch in a layer of finite thickness gives the key to understand the shallow compression in the hangingwall plate. Its occurrence is investigated in this paper using elastic finite element analysis for clarity, but with some reference to elastoplastic models which may include friction. It is shown that in normal faulting potential angular mismatch is more complicated than originally recognised since geometrical asymmetry between footwall and hangingwall plates gives rise to a smaller opposing contribution.

Investigation of the stresses associated with planar normal faulting is based on an elastic model of faulting of 1000 m throw. This simple approach demonstrates the nature and origin of the associated stress distributions with greatest clarity. Faulting actually takes place by a series of sudden movements of a few metres at most accompanied by intervening periods of slow creep and ongoing sediment loading. However, the elastic modelling is linear to an accuracy of 1% up to 1000 m throw so that the same stresses could result from a cumulative succession of incremental movements without significant error. The model is compatible with the flexural-cantilever model of planar faulting (Kusznir et al., 1991) except that the pure-shear deformation of the ductile lower crust is not incorporated; this may cause a long-wavelength depression of ~20 m which would not significantly affect the mechanics of the upper crustal faulting.

2. Modelling planar normal faulting

The finite element grid used to demonstrate and explain the shallow compression represents a two-dimensional normal-faulted elastic layer of 750 km long and 12 km thick overlying an inviscid substratum (Fig. 1). The planar fault initially dips at 45° and is
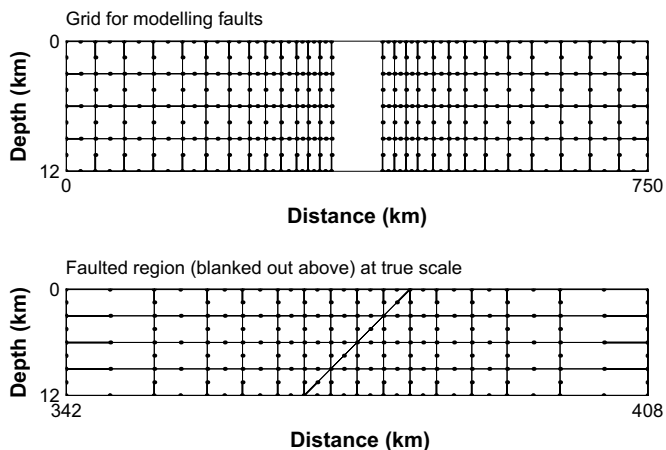
Fig. 1. Isoparametric finite element grid used for modelling the 750 km long faulted layer (Figs. 2 and 3). The nodes are represented by solid dots. The whole grid, except the regions adjacent to the fault, is shown above. The horizontally enlarged faulted region is shown below. This grid has also been subdivided into two separate independent grids of the hangingwall and footwall plates in order to investigate the mechanics of the faulting (Figs. 4–6, 8 and 9).
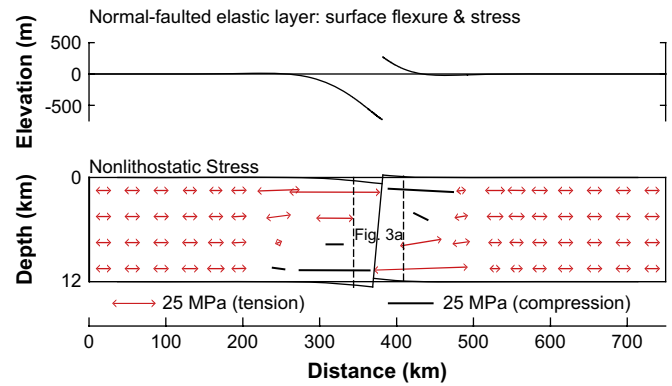
Fig. 2. Surface flexure and nonlithostatic principal stresses at the centres of selected elements produced by 1088 m extension of the 750 km long layer fixed to zero horizontal displacement at its left edge. The region in the vicinity of the fault extending between the vertical dashed lines is shown in more detail in Fig. 3. The complementary near-vertical principal stresses are too small to display in this figure but are visible in the region of the fault (Fig. 3).

frictionless. Young's modulus is 0.9×10^5 MPa and Poisson's ratio is 0.27. The fault is modelled by the dual node technique which simulates the influence of earth pressure in forcing the fault planes to remain everywhere in contact. Plane strain is assumed. The layer is fixed horizontally at its left end and is extended by 1088 m at its right end, producing 1000 m displacement on the normal fault and associated flexure of the two plates.

Isostatic loading at the surface is applied assuming a uniform crustal density of 2750 kg/m^3 and sediments of density 2350 kg/m^3 filling the half graben to datum, giving anomalous loads of 2750 kg/m^3 for the footwall uplift and 400 kg/m^3 for the half graben. Since the isostatic restoring forces are in equilibrium with the equal and opposite vertical force distributions on the opposing fault planes, the footwall uplift and subsiding half graben must remain in local lateral isostatic equilibrium with each other as the fault moves.

The following sign conventions are adopted. Displacements are positive upwards although depths are shown as positive in the figures. Rotations, as viewed in the figures, are positive anticlockwise. Potential mismatch affecting the adjacent fault planes is defined as the rotation of the hangingwall minus that of the footwall.

The simple features of the planar normal faulting are shown in Figure 2. The surface flexure profile shows that a half graben forms which is wider and shows larger vertical displacement than the complementary footwall uplift. This results from the contrasting isostatic loading on opposite sides of the fault. The nonlithostatic principal stresses are shown below at the centre of selected elements. These represent the actual principal stresses minus the lithostatic pressure which increases uniformly with depth beneath the datum of the original horizontal top of the layer. The stresses referred to throughout the paper are nonlithostatic principal stresses except where otherwise stated. The dip of the fault plane shallows by 0.541° during faulting to a final dip of 44.459° as the surfaces of the plates adjacent to the fault steepen by the same amount. The shallowing of the fault plane is approximately proportional to throw.

The stress distribution (Fig. 2) shows nearly horizontal principal stresses only since the complementary near-vertical principal stresses are too small to display. Towards the edges of the model outside the regions of faulting and strong flexural deformation, a relatively uniform horizontal tension of about 8.9 MPa is seen throughout the vertical thickness of the layer. This represents the stretching of the layer related to the faulting. Nearer to the fault, large bending stresses locally exceeding 50 MPa appear to
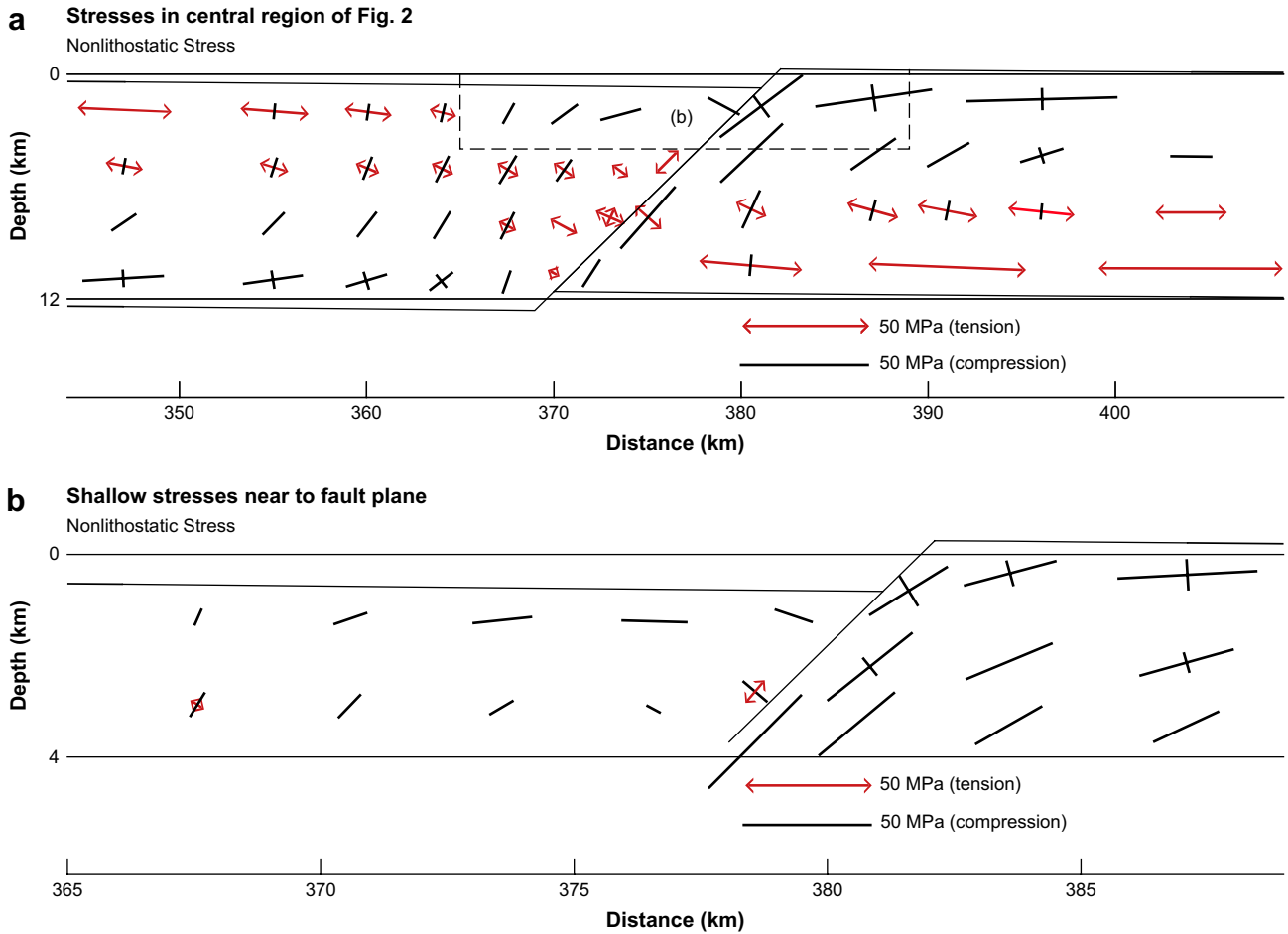
Fig. 3. The nonlithostatic principal stresses in the immediate vicinity of the fault (Fig. 2), plotted at true scale: (a) Stresses are shown at the centres of selected elements for the whole thickness of the layer. Note the sub-horizontal compression near the top of the hangingwall plate within about 12 km of the fault, the large compressive stress parallel and adjacent to the footwall, and the tensile stresses adjacent to the hangingwall. (b) The shallow stresses down to 4 km depth are shown at depths of 0.63, 2.37 and 3.63 km beneath the top of the deformed layer, averaged horizontally for each element from the values at the upper and lower Gauss points. This shows how the shallow compression increases towards the top of the hangingwall plate. The location of (b) is outlined by dashed lines in (a).

dominate. Shallow tension and deep compression occur beneath the downflexed half graben and vice-versa beneath the footwall uplift. The stretching and bending stresses are superimposed. Stretching and bending produce the only obvious stress visible as the scale is too small to see the detail near to the fault. These stresses are well understood but they do not represent the complete stress regime even in the region shown.

3. Shallow compressive stresses above the hangingwall

The stresses at the centre of selected elements in the vicinity of the fault are shown in Fig. 3a. An enlarged plot down to 4 km depth (Fig. 3b) shows stresses at the Gauss-point[1] depths of 0.63 and 2.37 km below the top of each element, averaged horizontally for each element. In contrast to the horizontal stresses at distance (Fig. 2), the stresses swing parallel to the friction-free fault near to it. These plots reveal two occurrences of compressive stress which do not fit into the scenario of stretching and bending stresses

described in Section 2, namely shallow sub-horizontal compression above the hangingwall and a large fault-parallel compression adjacent to the footwall. Fault-parallel tension occurs along the hangingwall.
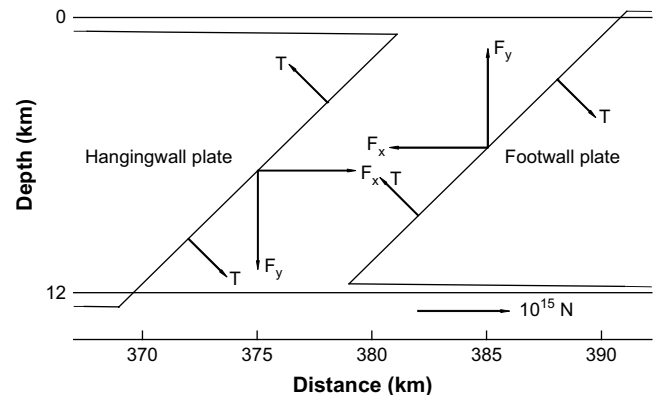
Fig. 4. Resultant irrotational linear forces (*F*) and couples (*T*) acting on the two fault planes as extracted from the finite-element modelling of the elastic model (Figs. 2 and 3). The forces and couples are represented, to the same scale, by the vertical and horizontal components of the single resultant irrotational forces shown at the mid-points and as single couples with forces acting at the quarter-points. In reality the forces are distributed in a complicated way over the nodes along each side of the fault (see Fig. 1).

---

[1] The Gauss points are special locations within elements used for numerical integration in the finite element computations. Rectangular elements have four Gauss points and triangular elements have three. Stresses are computed at the Gauss points and these can be averaged to give the stresses at the centre of an element.

The shallow sub-horizontal compressions above the hangingwall (Fig. 3a and b) extend for nearly 14 km from the fault where only sub-horizontal tension would be expected from plate bending and stretching. The largest compression at a Gauss point of 25 MPa occurs at 0.63 km depth in the plate at about 5 km horizontal distance from the fault. Fig. 3b shows that these sub-horizontal stresses increase upwards towards the surface and are restricted to a depth of about 4 km within the hangingwall plate. Linear extrapolation from the displayed stresses computed at the Gauss points indicates that a maximum compression of 33 MPa occurs at the plate surface about 5 km from the fault. These compressions are attributed in Section 4 to suppression of angular mismatch of the fault planes. Such stresses are large enough to overcome the expected tensions at the top of the hangingwall plate near to the fault, but it is shown in Section 5 that they occur less visibly elsewhere in the model, with compression at the top of the plate on both sides of the fault, and complementary tension on both sides near its bottom.

Large fault-parallel compressive stresses occur in the footwall plate immediately adjacent to the fault (Fig. 3b). Such compressions occur along the length of the footwall, with maximum computed amplitude at the Gauss points adjacent to the fault, dying off away from the fault. A maximum value of 51 MPa occurs at 3.7 km depth, dying off along the fault to 36 MPa near the surface and 9 MPa near the base of the plate. In contrast, smaller fault-parallel tensions occur adjacent to the hangingwall, peaking at 17 MPa at 5.7 km depth and dying off to small compressions at the top and bottom. These fault-parallel stresses are explained in Section 5, where they are shown to originate from superposition of bending and mismatch stresses.

4. Origin of anomalous shallow compression and deep tension at normal faults

In the finite element method, the equal and opposite tractions acting on the opposing fault planes are represented by nodal forces. These forces must act perpendicular to the fault plane as zero friction is assumed. The forces have been extracted from the results of the elastic modelling (Figs. 2 and 3). In addition to the irrotational forces, a substantial couple acts on each fault plane. The horizontal and vertical components of the resultant irrotational force (F_x and F_y respectively) and the total couple T acting on the hangingwall fault plane are as follows: $F_x = 1.070 \times 10^{11}$ N, $F_y = -1.080 \times 10^{11}$ N (acting downwards), and $T = 4.988 \times 10^{14}$ N m (acting anticlockwise). Equal but opposite forces and an opposite couple act on the footwall. This situation is illustrated in Fig. 4, which shows the faulted edges of the two plates (Figs. 2 and 3) separated by about 9 km, with only the resultant force components and torques illustrated for simplicity. The components of the resultant forces are shown at the mid-points and the forces producing the couples are shown at the quarter-points on the same scale as F_x and F_y. The horizontal forces F_x are in equilibrium with the horizontal forces at the distant edges of each plate related to the extension of the layer. The vertical forces F_y are the edge forces which cause the throw of the fault and are balanced by the vertical isostatic forces acting at nodes along the surface of the appropriate plate. The role of the couple T is to rotate the fault planes in opposite directions so that they remain everywhere in contact.

In order to test the mismatch quantitatively, the equal but opposite irrotational horizontal and vertical edge forces acting on each fault plane have been applied *separately* to each plate in the absence of the couples but including identical isostatic surface loading as in the relevant part of the original model (**stage 1**). The edges of both models distant from the fault have been assigned zero horizontal displacement. The results of these two separate computations produce similar but not identical flexure to the

Table 1
Fault plane dips.

	Start	End	Rotation
Original model (Figs. 2 and 3)	45.000°	44.459°	**−0.541°**
Downbending of free hangingwall (Fig. 6)	45.000°	44.340°	−0.661°
Rotation produced by couple (hangingwall)	44.340°	44.460°	+0.121°
Total rotation of hangingwall	45.000°	44.460°	**−0.540°**
Upbending of free footwall (Fig. 6)	45.000°	44.563°	−0.438°
Rotation produced by couple (footwall)	44.563°	44.460°	−0.103°
Total rotation of footwall	45.000°	44.460°	**−0.540°**

original model. Both the fault planes rotate clockwise about a horizontal axis along the strike of the fault plane so that their dips are reduced in conformity with the flexural bending. However, the hangingwall rotates 51% more than the footwall (Table 1). As a result the two fault planes diverge downwards by an angle of 0.223°. This represents the mismatch caused by the difference between the flexure affecting each plate.

In reality, the hangingwall and footwall are forced together under the downward increasing lithostatic pressure (Bott, 1996). This process produces the couple T which gives rise to horizontal compression and deep tension in the layer. The simulation of the faulting process is completed for each of the two plates as deformed by the linear forces in **stage 1** above by treating them as unstressed. Fixing their distant edges to zero horizontal displacement and using the same pattern of isostatic loading, the two plates are further separately deformed by the equal but opposite couples T (**stage 2**). The resulting dips of the fault planes both now agree with that of the original deformed model to an accuracy of rotation of 0.2% (Table 1). The upthrow and downthrow at the surface also
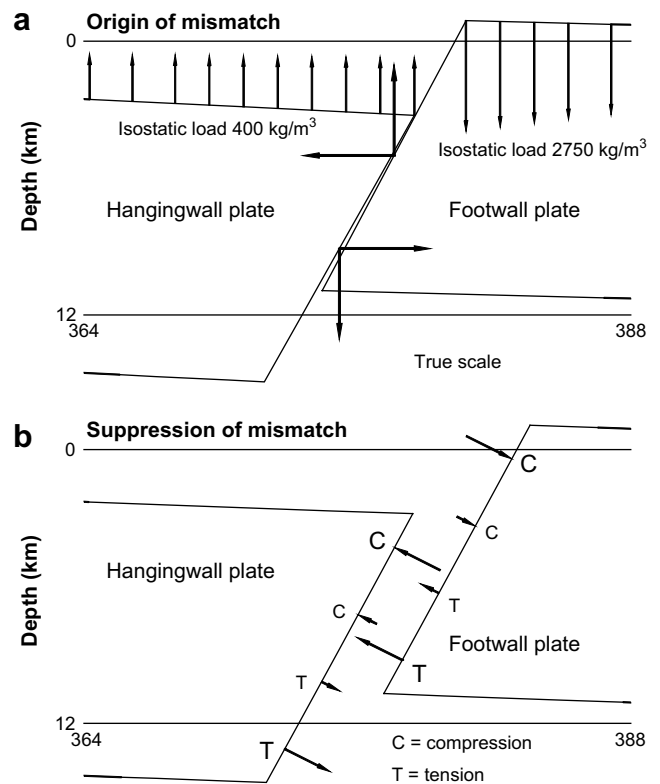
Fig. 5. Visual demonstration (a) of the origin of mismatch by separate deformation of hangingwall and footwall plates by horizontal and vertical forces extracted from the modified fault model but in the absence of couples; and (b) of its correction by application of the couples to the deformed plates (see text for details).

agree with the original model to within 1 and 2 m respectively. Thus splitting the normal faulting process into these two stages accurately simulates the original model, demonstrating that the couple corrects the potential mismatch, being an essential part of the normal faulting process.

The origin and suppression of mismatch are demonstrated visually in Fig. 5. This uses a modified model which develops much larger mismatch to enable clear display. The new model is 600 km long and is extended by 2500 m at its left edge with the fault dipping at 63.4° (=arctan2), but is otherwise identical to the original model (Fig. 1). The two plates have been separately deformed as in **stage 1** above by the irrotational forces acting on the fault nodes extracted from the modified model. They have been juxtaposed at the top of the hangingwall to display the mismatch of 1.33° (Fig. 5a). The isostatic restoring pressures acting at selected nodes on top of the plates (Fig. 5a) are proportional to the product of vertical displacement and the isostatic loading density and consequently are largest on the footwall plate near to the fault.

In **stage 2**, the deformed plates resulting from **stage 1** were subjected to the opposite rotational forces (couples) acting perpendicular to each fault plane (Fig. 5b). These are shown as forces acting on selected nodes. They pull the plates apart at the top producing compression on both sides and force them together near the bottom producing tension as shown.

5. Bending and mismatch suppression stresses

The two stages described above enable separation of stresses caused by stretching and bending from those caused by mismatch suppression, at least approximately. The separated stresses are shown in Fig. 6, with a small gap between the plates to enable the stresses near the fault to be seen clearly and to emphasize that the computations have been done separately for each plate. Fig. 6a shows the isolated bending and stretching stresses caused by the irrotational forces acting on the fault planes whereas Fig. 6b shows the separated mismatch suppression stresses produced by the couples.

5.1. Bending stresses

Bending stresses (Fig. 6a) are parallel to the upper and lower surfaces near to the top and bottom of each plate, and form an approximately anti-symmetrical pattern about a vertical plane through the centre point of the fault. The bending stresses are prominent in the regions of large flexure. The tensional bending stresses decrease to negligible values adjacent to the fault near the top of the hangingwall and bottom of the footwall. The small pervasive tension due to stretching causes maximum tensions to exceed maximum compressions on both sides of the fault. The compressive bending stresses swing round inside the obtuse angles at the top of the footwall and bottom of the hangingwall. They run parallel to the friction-free fault plane along its length on both sides, as seen in Fig. 6a which is plotted at true scale. The fault-parallel compressive stresses reach peak amplitudes of 25 MPa near the top of the footwall and the bottom of the hangingwall.

5.2. Mismatch suppression stresses

The mismatch suppression stresses are also predominantly horizontal except near to the fault (Fig. 6b). They are compressive
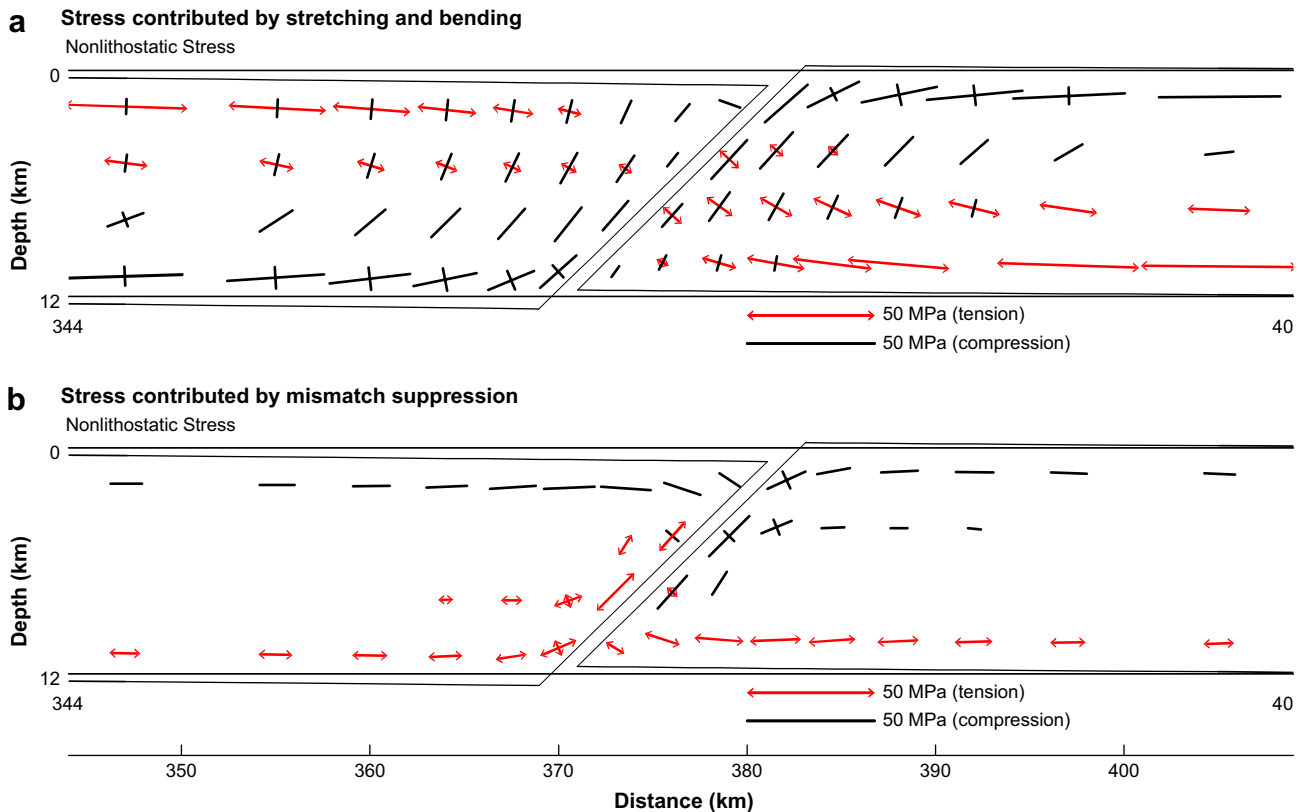
Fig. 6. Nonlithostatic stress field for the separately computed models for hangingwall and footwall plates which are shown together but with a small lateral separation for clarity. The stresses are shown for each of the two stages into which the faulting process has been artificially split to illustrate the mechanics of the faulting: (a) **Stage 1**: The stresses resulting from application of the equal but opposite irrotational linear forces without the couples as applied to the separated fault planes. This shows stresses related to stretching and bending only. (b) **Stage 2**: The separated mismatch suppression stresses produced by application of the couples to the deformed but stress free models in (a).
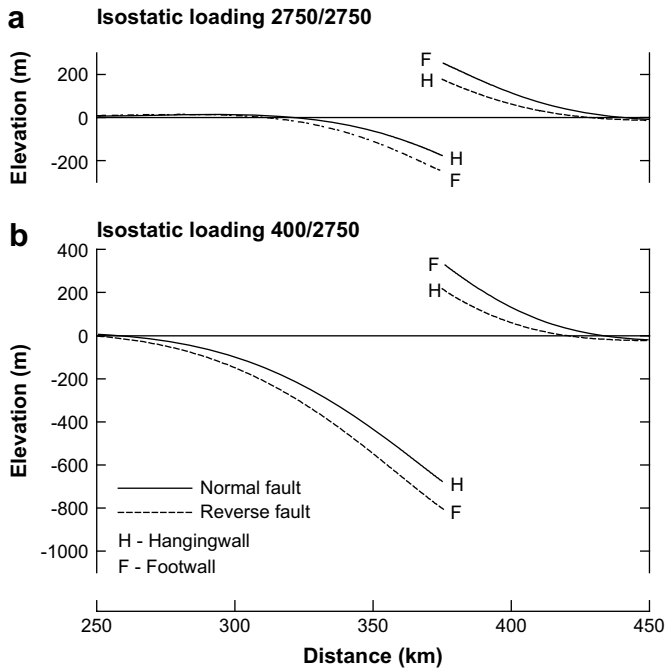
Fig. 7. The flexural profiles across comparable normal and reverse faults developing resultant vertical forces of equal magnitude acting on their fault planes. The reverse faults dip in the opposite direction so that both downthrown plates are to the left and both upthrown plates are to the right. Profiles are shown in (a) for isostatic loading of density of 2750 kg/m^3 above both plates, and in (b) for isostatic loading densities of 2750 kg/m^3 (upthrown plates) and 400 kg/m^3 (downthrown plates).

Table 2
Vertical displacement (throw) and rotation at the free edges of the separated fault plates in response to equal resultant vertical edge forces acting downwards on the fault plane nodes, with isostatic loading of 2750 kg/m^3 throughout. The throw is computed at the mid-point of the fault planes. The asterisks denote that all isostatic loading vertically above the fault plane is omitted.

	Throw (m)	Rotation (deg)
Hangingwall (normal)	−155.3	−0.224
Footwall (reverse)	−294.0	−0.444
Hangingwall* (normal)	−292.1	−0.441
Hangingwall (reverse)	155.6	−0.225
Footwall (normal)	293.0	−0.442
Hangingwall* (reverse)	293.5	−0.439

near the top of the layer and tensile near the bottom. Their values are small in the central region of the layer except near to the fault. They are somewhat larger along the top of the hangingwall plate than along its bottom, and vice-versa for the footwall plate. They have an approximately symmetrical pattern about the central vertical plane, in contrast to the anti-symmetrical bending stresses. The horizontal stresses reach 27 MPa compression near the top of the hangingwall plate and 27 MPa tension near the bottom of the footwall plate. The comparable stresses at the bottom of the hangingwall and top of the footwall are 20–30% smaller. They decrease in magnitude to less than 1 MPa at about 170 km from the mid-point of the fault in the hangingwall plate and at about 86 km in the footwall plate, becoming insignificant a short distance beyond. The mismatch stresses bend round inside the obtuse angles at the fault in the same way that the bending stresses do, continuing parallel to the fault planes along their length (Fig. 6b). This produces fault-parallel compressive stress of up to 26 MPa adjacent to the footwall and tensile stress of up to 24 MPa adjacent to the hangingwall.

5.3. Synthesis

The stresses shown in Fig. 6 approximately represent the two contributions from bending/stretching and from mismatch suppression contributing to the original elastic stress distribution (Figs. 2 and 3). They are not exact contributions because of non-linearity in splitting the computation into two stages, particularly associated with the acute angles at the faulted end of the plates. However, they are adequate to give insight into the origin of the stresses. Figs. 3a, 6a and b cover the same region on the same true scale and the following conclusions can be drawn from comparison of these. *First*, the horizontal mismatch compression at the top of the hangingwall and the corresponding mismatch tension at its base outweigh the other stresses of opposite polarity in these regions. Elsewhere, their dominant presence is swamped by the other stresses. *Second*, the large shallow horizontal compressions and deep tensions in the footwall plate occur where the bending and mismatch stresses reinforce each other; correspondingly smaller shallow compressions and deep tensions occur in the hangingwall plate where they are of opposite polarity. *Third*, the large fault-parallel compressions along the faulted edge of the footwall plate occur where the two contributions reinforce each other whereas the smaller tensions along the edge of the footwall plate occur where the bending and mismatch contributions are of opposite polarity.

The strong contrast between the stress environment along hangingwall and footwall is directly related to the change in polarity of the isostatic restoring forces across the fault at the surface (Fig. 5a) and the opposite vertical forces acting on the adjacent fault planes (Fig. 4). This contrast is further discussed in Section 8.1.
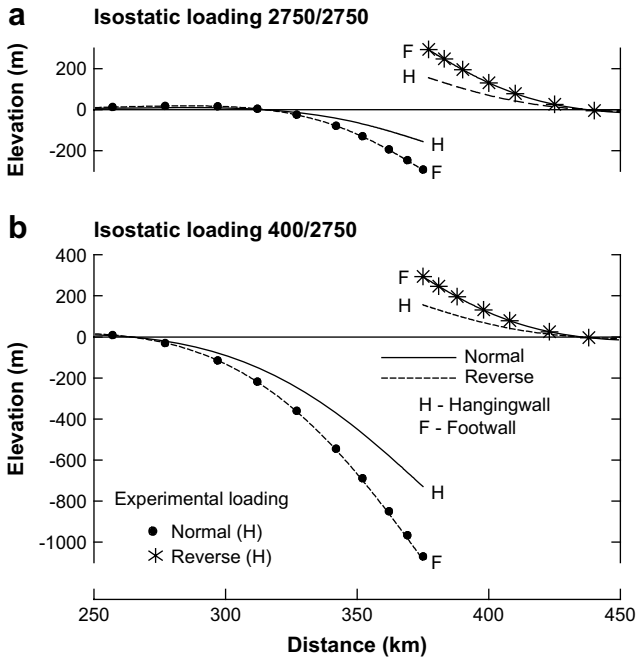

Fig. 8. Comparison of the flexural profiles for the separated hangingwall and footwall plates deformed at their edges by the irrotational vertical and horizontal forces extracted from the original models of the faulting shown in Fig. 7. Profiles are shown in (a) for models with isostatic loading of 2750 kg/m^3 above both plates as in Fig. 7a, and in (b) for models with differential loading as in Fig. 7b. The solid dot and asterisk symbols represent the experimental models of the hangingwall plates which omit isostatic loading above the fault.

Table 3
Tabulation of the independently computed throw and rotation of the pairs of hangingwall and footwall plates for normal and reverse faults with the same isostatic loading of 2750 kg/m^3 on both sides (rows 1 and 2) and differing isostatic loading (upthrown side 2750 kg/m^3 and downthrown side 400 kg/m^3). In column 1, (s) denotes same isostatic loading on both sides and (a) denotes different loading. As in Table 2, the asterisks denote the absence of isostatic loading vertically above the hangingwall. Column 2 shows whether the plate is hangingwall (H) or footwall (F). The final three columns show the contributions to mismatch: A denotes the effect of differing isostatic load densities above the hangingwall and footwall plates, B denotes the geometrical contribution, and A + B denotes the resultant mismatch.

Fault type	Left plate (downthrown)			Right plate (upthrown)			Mismatch		
	Load (kg/m^3)	Throw (m)	Rotn (deg)	Load (kg/m^3)	Throw (m)	Rotn (deg)	A (deg)	B (deg)	A + B (deg)
Normal(s)	2750H	−155	−0.224	2750F	+293	−0.442	0.000	+0.218	+0.218
Reverse(s)	2750F	−294	−0.444	2750H	+156	−0.225	0.000	−0.219	−0.219
Normal[*]	400H	−1071	−0.982	2750F	+293	−0.438	−0.544	0.000	−0.544
Reverse[*]	2750F	−1084	−1.004	400H	+294	−0.447	−0.557	0.000	−0.557
Normal(a)	400H	−729	−0.661	2750F	+293	−0.438	−0.544	+0.321	−0.223
Reverse(a)	2750F	−1084	−1.004	400H	+156	−0.227	−0.557	−0.219	−0.776

6. The flexural mechanics of planar faulting and the origin of mismatch

The origin of mismatch is most easily explored by comparing the surface flexure profiles associated with normal and reverse faults
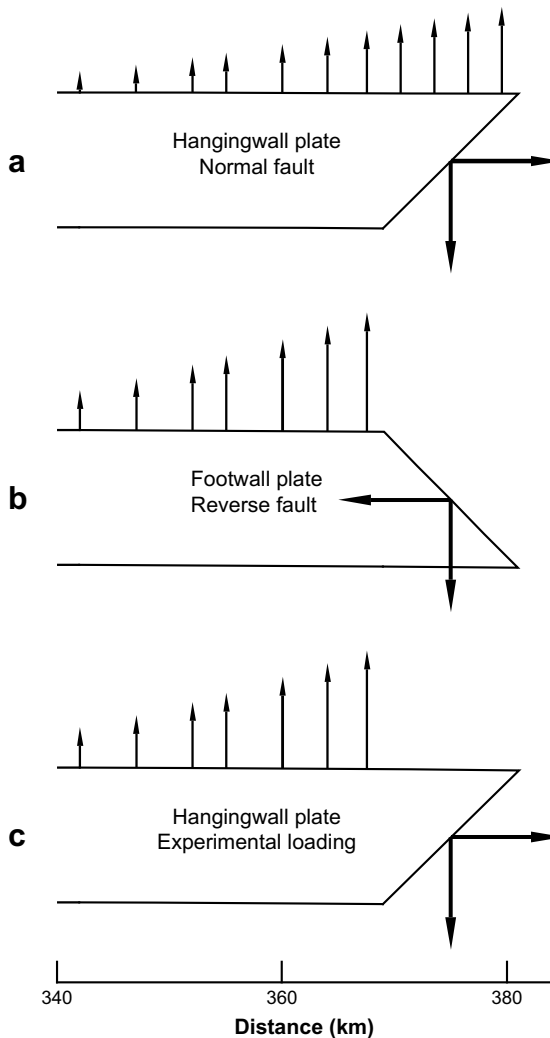
Fig. 9. The contrasting distributions of isostatic loading pressure (denoted by thin arrows) acting upwards (a) on the surface of the separated downthrown normal-faulted hangingwall plate, and (b) on that of the reverse-faulted footwall plate, for the models shown in Fig. 8a. The thick arrows show the resultant forces acting on the separated fault planes which cause the flexure; these are not on a comparable scale to the isostatic pressures. (c) shows the effect of omitting the isostatic loading vertically above the normal-faulted hangingwall (a), when the loading becomes identical to that acting on the reverse-faulted footwall plate (b).

for both equal and unequal isostatic loading (Fig. 7). Four models are presented using the original finite element grid (Fig. 1) except that reverse faults dip in the opposite direction so that the left plates are downthrown and the right plates upthrown in all the models. These models include the original normal-faulted model (Fig. 2), an equivalent reverse-faulted model with the same unequal isostatic loading, and normal- and reverse-faulted models with the same isostatic loading density of 2750 kg/m^3 on both plates. The new models have been designed so that the resultant vertical forces acting on the fault planes are equal in magnitude to those of the original normal-faulted model. The flexural profiles are shown for equal isostatic loading in Fig. 7a and for differential loading in Fig. 7b. The most noticeable feature of the profiles is that the vertical displacement of each footwall is greater than that of the comparable hangingwall for the same isostatic loading. Fig. 7a shows anti-symmetrical profiles for footwalls and for hangingwalls.

The plates in each model were then separated as in Section 4. The separated plates were deformed by fixing the distant edges and applying the vertical and horizontal irrotational forces on the fault nodes as extracted from the four models shown in Fig. 7. The profiles for each pair of separated plates are shown in Fig. 8.

First, we focus on the results for the separated plate models with the same isostatic loading on both plates (Fig. 8a and Table 2). The profiles are anti-symmetrical, with reverse upthrow equalling normal downthrow to ±1 m and vice-versa. For the separated normal fault plates, footwall upthrow exceeds hangingwall downthrow by 89% and footwall rotation exceeds that of the hangingwall by 97%. Almost the same throws, but the other way round, apply to reverse faulting (Table 2). The mismatch calculated from the rotations (Tables 2 and 3) is +0.218° for the normal fault and −0.219° for the reverse fault, almost equal but opposite. This mismatch cannot be caused by unequal isostatic loading densities nor can it be significantly attributed to the influence of the horizontal irrotational forces acting on the fault plane since these forces would increase the magnitude of mismatch for reverse faulting but reduce it for normal faulting. It must therefore arise mainly from the anti-symmetrical geometry of the plates. It will be referred to as geometrical mismatch.

The most obvious hypothesis is that the geometrical mismatch is caused by the differing distributions of isostatic restoring pressures acting on the upper surfaces of the hangingwall and footwall plates. These pressures extend above the length of the fault along the hangingwall plate but do not occur above the fault along the footwall. To demonstrate this, the isostatic pressure, which is proportional to the vertical displacement at the surface, is shown at the same arbitrary scale along the normal-faulted downthrown hangingwall and the reverse-faulted downthrown footwall in Fig. 9a and b. The total integrated isostatic pressure acting on the plate surface yields a force which must be equal to but opposite from the resultant vertical force acting on the fault plane. But the distribution of the pressure differs between the plates. Absence of

isostatic loading above the fault along the footwall plate is compensated by substantially larger pressures beyond the fault. The bending moment acting along each plate arises from the combined effect of the surface isostatic pressure distribution and the equal but opposite vertical force acting on the fault plane. Fig. 9a and b shows that the bending moment at equal horizontal distances from the mid-point of the fault plane must be substantially larger along the footwall plate than along the hangingwall plate. This causes greater vertical flexural displacement along the footwall than the hangingwall and hence greater rotation.

This hypothesis is further tested by using experimental models in which the isostatic loading pressures, represented by nodal forces, are omitted vertically above the normal and reverse hangingwalls as shown in Table 2 (rows 3 and 6) and Figs. 8a and 9c. This shows that if the isostatic loading has the same horizontal distribution above hangingwall and footwall plates (both being either downthrown or upthrown), then their flexural profiles, throw and rotation all become effectively equal in magnitude to each other. These results show that the differing distribution of isostatic restoring pressures above hangingwall and footwall is the primary cause of geometrical mismatch. The full computations of the mismatch for equal isostatic loading are summarized in Table 3, rows 1 and 2.

Second, analysis of mismatch has been undertaken for the more complicated models of normal and reverse faulting with differing isostatic loading on opposite sides of the fault (Fig. 7b). The plates were separated and deformed by the vertical nodal forces on the fault plane in the same way as in the simple model above, the results being shown in Fig. 8b and Table 3, rows 5 and 6. The resulting rotations at the edge of the plates yield estimates of the total mismatch of $-0.223°$ for the normal fault and $-0.776°$ for the reverse fault. These are consistent with the couples acting on the fault plane keeping the plates in contact, which are 0.4988×10^{15} N m for normal faulting and 1.7084×10^{15} N m for reverse faulting. The reverse mismatch angle and couple are both 3.4 times the comparable values for a normal fault. This agrees with the magnitude of the mismatch stresses which when isolated (as in Fig. 6b) are also 3.4 ± 0.2 times larger in the reverse model than the normal model. Whereas the bending stresses dominate in normal faulting, it is the mismatch stresses which dominate in reverse faulting.

The two types of mismatch combining to give the above result can be isolated from each other by omitting the isostatic loading above the downthrown normal-faulted plate and the upthrown reverse-faulted plate above the hangingwall (Fig. 8b, Table 3 rows 3 and 4). This eliminates the geometrical mismatch and isolates the contribution caused by the different isostatic loading on opposite sides of the fault. The values of mismatch resulting from differential isostatic loading are $-0.544°$ for the normal fault and $-0.557°$ for the reverse fault, being nearly equal. Subtracting these values from the total mismatch yields geometrical mismatch of $+0.321°$ for the normal fault and of $-0.219°$ for the reverse fault (Table 3, rows 5 and 6). The geometrical mismatch is of opposite sign for the normal and reverse faults and is of larger magnitude for the normal fault because of the larger vertical displacement of the hangingwall. The large difference in total mismatch thus results from the two contributions having the same negative sign in reverse faulting but opposite signs in normal faulting.

7. Shallow hangingwall compression in other models of normal faulting

A variety of models of normal faulting have been studied to explore the extent of mismatch suppression stresses. Some of these are from previous elastoplastic modelling including unpublished work. Most of the models display shallow compression above the hangingwall within a few kilometres of the fault trace and are briefly described here.

The elastic model has been modified for fault dips ranging from 31° to 71° in addition to the original 45°. These models all have a throw of 1000 m. They all display shallow compression in the hangingwall plate within 8–12 km of the fault trace. Within the range 50–60°, the maximum compressive stress exceeds that of the original model by up to about 8%, and beyond this range it falls off in both directions to values up to 35% smaller at 31° and 71°. All these models show fault-parallel compression adjacent to the footwall.

Bott (1997) used the Von Mises failure criterion to approximate Byerlee-type failure in modelling normal faulting in the brittle upper crust. Subsequent models have been computed using the Coulomb–Navier failure criterion which accurately represents the Byerlee strength profile. These assume friction of 0.75 and hydrostatic water pressure in the cracks although the fault itself remains frictionless. In all these models, the fault dips at 63.4°. They include models with varying layer thickness and graben infill density. Each has been extended by 200 m increments until failure occurs locally across the whole thickness of the plate. Nearly all the models show actual shallow sub-horizontal compression above the hangingwall down to about 2 km depth and out to about 5–12 km from the fault. The elastoplastic results are compared with those for an otherwise comparable elastic model dipping at 63.4° after extensions of 800 m in Fig. 10a and b. Both have been computed using zero deviatoric z-stress rather than plane strain because the stability of solution is better in the elastoplastic modelling. The deviatoric rather than nonlithostatic stress is shown since this is related to the failure criterion (failure is indicated by asterisks in Fig. 10). The pattern of shallow stresses is similar in both models, although the
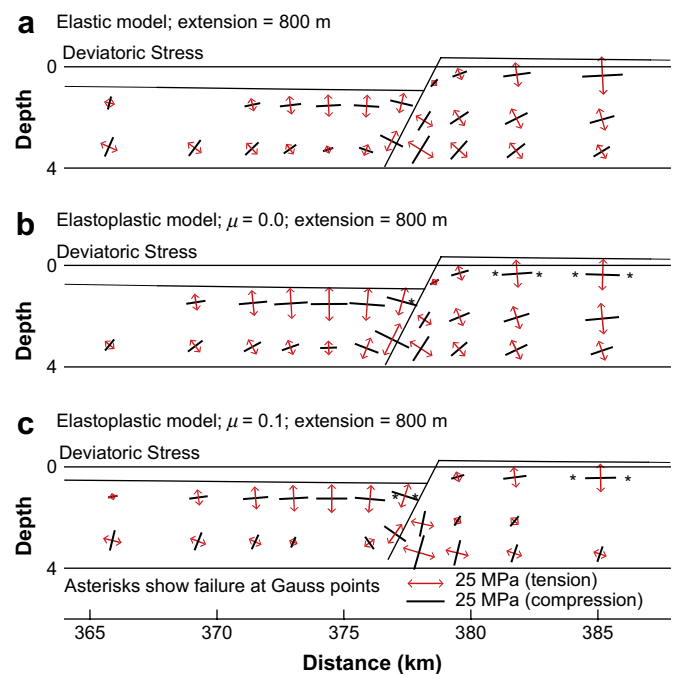
Fig. 10. Deviatoric stresses at 800 m extension are shown for (a) an elastic model, (b) a similar elastoplastic model without friction, and (c) an elastoplastic model with friction of 0.1. These models differ from those shown in Figs. 1–3 in being 600 km long with a fault dipping at 63.4°, but elastic properties, layer thickness and isostatic loading are identical. Elastoplastic (compressive) failure is shown by asterisks at Gauss points where it occurs. A finite element formulation assuming zero deviatoric z-stress rather than plane strain has been used in all three models for reasons of computational simplicity in the elastoplastic modelling.

shallow compressions in the hangingwall plate are rather larger for the elastoplastic rheology.

Elastoplastic results are available for layer thicknesses of 8, 12 and 16 km, using the same graben infill density of 2350 kg/m³ (isostatic loading density 400 kg/m³). The shallow compressive stress above the hangingwall is present in all these models until extensional failure occurs locally across the whole thickness of the plate, when the fault movement effectively ceases. The maximum mismatch compressions increase with increasing thickness of the layer, as might be expected because of the greater length of the fault plane.

The dominant influence on the amplitude of the shallow compressive stresses above the hangingwall is the contrast in density between the half graben infill and the upper crustal basement. This is investigated using the simple elastic model (Fig. 1). Reducing this contrast to 200 kg/m³ (Fig. 2) increases the resultant compressive stresses by about 50%. Increasing the contrast to 600 kg/m³ reduces them comparably. The shallow compression above the hangingwall is small for a density contrast of 1000 kg/m³ and is about zero for water infill. When infill is absent so that the isostatic loading density is 2750 kg/m³ on both sides of the fault, there is a shallow tension of about 20 MPa in place of the compression above the hangingwall, indicating that the mismatch effect has reversed (Table 2). These elastic models indicate that the isostatic density differential across the fault is the most important factor in the origin of the mismatch stress.

A systematic study of friction on normal faulting has also been carried out. For a realistic value of effective friction of 0.1, which is equivalent to friction of 0.75 and fluid pressure of 0.867 × lithostatic pressure, shallow compression above the hangingwall is present at levels of about 65% of the friction-free case (Fig. 10c). For effective friction greater than 0.2, the mismatch compression is typically swamped by the high tension required to initiate faulting.

8. Applications

The elastic modelling described so far gives an overview of the stress distribution resulting from an extended period of faulting without taking into account a number of complications. In reality, faulting takes place by a series of sudden displacements of up to a few metres, possibly punctuated by periods when sediments may accumulate and slow creep may occur. A further complication is that bending and mismatch stresses characteristically reach large values which can probably be partially relieved by transient creep and local brittle fracture (Bott and Kusznir, 1984). Consequently, the bending and mismatch stresses may well relax to smaller values than shown in Figs. 2, 3, and 6. However, a general increase of the level of stress, with superposed fluctuations over the faulting cycle, would be expected to apply to the progressive development of a planar normal fault.

An important implication of mismatch and its suppression in planar faulting is that the flexural deformation of the hangingwall is reduced relative to that of a thin plate, and that of the footwall is correspondingly increased. Fig. 8 shows that the flexure of hangingwall is always significantly less than footwall with the same isostatic loading density. This is a factor which could be incorporated in the flexural-cantilever method (Kusznir et al., 1991) and other flexural studies of faulting to improve the accuracy of representation.

The present finite element approach can also model the variations of stress associated with the earthquake cycle of normal faulting. Preliminary computations yield similar estimates of the coseismic stress drop to those obtained by King and Cocco (2001) using dislocation theory. They also support the interpretation by

Muir-Wood and King (1993) and King and Muir Wood (1994) of the discharge of water following major normal fault earthquakes in terms of expulsion of water to the surface in response to the compressive stress rebound. This indicates that the pattern of fluid flow in the faulted layer responds to quite small changes of stress of much less than 1 MPa. Further discussion of these is outside the scope of this paper and the discussion below focuses on other aspects of fluid flow and wall rock structure including fault drag.

8.1. The stress environment near to the fault

As pointed out in Section 8.3, an abrupt change in the stress environment occurs across the fault plane. Fig. 11a shows a profile of nonlithostatic pressure across the fault at just over 4 km depth. This represents the anomalous pressure relative to the uniform increase of lithostatic pressure with depth. Along the profile, there is an abrupt increase of confining pressure of about 28 MPa across the fault plane from hangingwall to footwall, equivalent to that for a depth increase of 1 km. This is related to the change in polarity of isostatic loading pressure across the fault at the surface (Section 5.3 and Fig. 5). A minimum pressure occurs along the length of the hangingwall and a maximum along the footwall. The pressure jump across the fault decreases to a much smaller values towards the base of the faulted layer.

The deviatoric stresses at Gauss points near the fault are shown in Fig. 11b. Principal stresses are orthogonal to the friction-free fault plane. The fault-perpendicular nonlithostatic principal stress
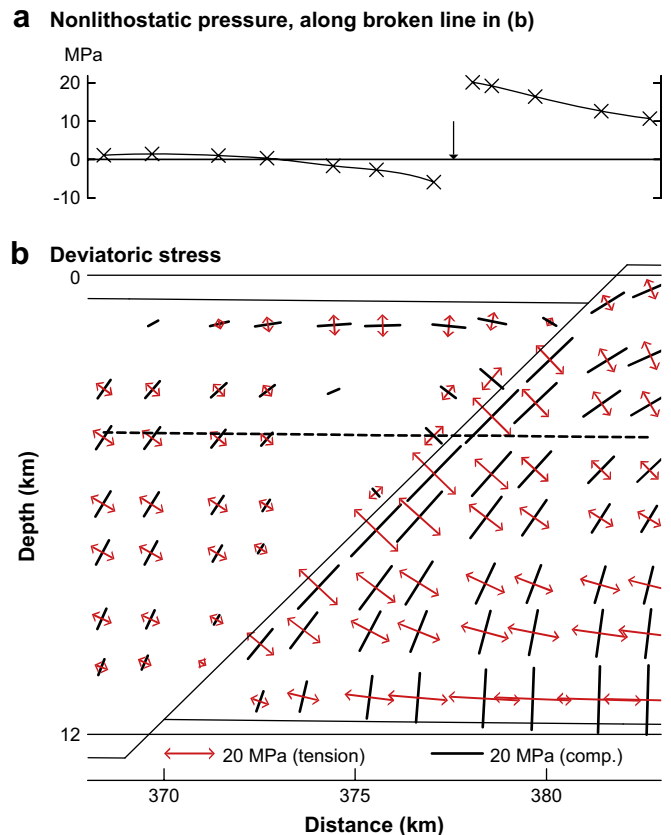

Fig. 11. The stress environment in the immediate vicinity of the fault, showing the abrupt transition in pressure and deviatoric stress across the fault plane. (a) Non-lithostatic pressure profile at 4.1–4.2 km depth, shown along the broken line in (b). The arrow marks the location of the fault plane. (b) Deviatoric stress shown at Gauss points except where too small to display.

(Fig. 3) is continuous across the fault plane but the deviatoric principal stress (Fig. 11b) is discontinuous and changes in polarity.

8.2. Fluid flow in the faulted layer

The developing stress field associated with ongoing normal faulting is relevant to the flow of fluids in the vicinity of the fault. The confining pressure in the faulted layer is the sum of the lithostatic pressure which increases linearly with depth and the nonlithostatic pressure (Fig. 11a). As the stress regime changes with progressive faulting, fluids will tend to migrate from regions of high nonlithostatic compression towards those of low compression. They also tend to rise towards the surface because of their much lower density than the country rocks, building up a head of pressure which may exceed the local confining pressure. This forces them upwards towards the surface through available passages, possibly assisted by the dyke emplacement mechanism of Anderson (1951) applied to the opening of cracks by high pressure fluids. Such cracks form preferentially perpendicular to the minimum principal stress.

Large nonlithostatic stresses affect the footwall plate beneath the footwall uplift where the mismatch and bending stresses reinforce each other (Figs. 3 and 6). The lower half of the plate is dominated by large tensions which reduce the confining pressure. This would be expected to encourage upflow of fluids from below. In contrast, large mainly horizontal compressions dominate the upper half of the plate, increasing the confining pressure and inhibiting upflow from the lower part of the plate towards the surface. Smaller nonlithostatic pressures dominate the hangingwall plate beneath the half graben (Fig. 3). These are compressive near the bottom and top of the plate and tensional or neutral in the intervening region.

The regions immediately adjacent to the fault are of particular interest because of the abrupt transition between extremes of confining pressure and deviatoric stress across the fault plane. The low pressure channel along the hangingwall (Fig. 11a) provides a passage for uprising hydrothermal fluids along the fault up to the surface. The hot fluids, in equilibrium with the confining pressure deep within the layer, would build up a considerable head of excess pressure at shallow depths enabling them to break through the shallow compression to the surface along the fault plane and the region immediately adjacent to it. The presence of such stress-dependent pressurized rising fluids may be a significant factor in weakening the zone adjacent to the hangingwall, providing a primary mechanism for fault-zone weakening by fluids (Rutter et al., 2001). Reaction of these hot rising hydrothermal fluids with feldspar and other minerals may contribute to formation of fault gouge.

In the narrow zone adjacent to the footwall, the large fault-parallel nonlithostatic compression increases the confining pressure along the length of the fault, peaking at the fault plane itself (Figs. 3 and 11a). This would be expected to inhibit fluid flow across the fault at all depths except possibly near the bottom of the plate where the compression is weakest. The high pressure combined with maximum fault-parallel deviatoric compression adjacent to the fault would inhibit any flow into the footwall from the low pressure channel along the fluid-saturated hangingwall. The small amount of fluid which may be present along the footwall may possibly flow slowly upwards along the fault which is perpendicular to the principal deviatoric tension (Fig. 11b).

8.3. Wall rock structure

The hangingwall and its immediate vicinity at shallow depth within the plate are particularly vulnerable to brittle fracture because of the low confining pressure and presence of pressurized warm rising fluids. This region may be affected by two types of fracture. First, fluid pressure may open pre-existing or new cracks preferentially orientated perpendicular to the deviatoric principal tension, which is parallel to the fault (Fig. 11b). Second, the fault-perpendicular principal deviatoric compression originating from mismatch suppression may be relieved by Coulomb–Navier fracture along conjugate fault planes subtending 45° or less to the principal deviatoric compression. The preferred angles are probably close to ±45° because of the high fluid pressure which may almost annul the friction. Since the fault dips at about 45°, there will be a steeper nearly vertical fracture plane subtending 45° or slightly more anticlockwise from the fault plane with sinistral displacement and a plane of small dip subtending 135° or slightly less, with dextral displacement.

Both types of fracture may use suitably orientated pre-existing planes of weakness. Tensile fractures would cluster around the perpendicular direction and Coulomb–Navier fractures subtending 45° or slightly more and 135° or slightly less from the fault plane. The Coulomb–Navier failure involves shortening perpendicular to the fault plane and also equivalent extensional strain parallel to it. Such extension must occur upwards towards the free surface.

Fig. 10 shows that the deviatoric compression is sufficient to cause elastoplastic Byerlee-law failure for fluids at hydrostatic pressure out to a distance of 1 km from the fault along the shallow hangingwall plate. However, the hot pressurized fluids rising along the shallow hangingwall would be expected to exceed the local confining pressure from time to time, greatly reducing the strength below the Byerlee value and relieving the mismatch stress along the hangingwall for much smaller values of deviatoric stress than those displayed in Fig. 10b and c. Hence release of mismatch strain probably occurs mainly in the weak region adjacent to the hangingwall during the repeated cycles of fault movement.

In contrast to the hangingwall, larger fault-perpendicular deviatoric tensions occur along the footwall. These peak at mid depths and generally decrease away from the fault plane. The shallow footwall is much stronger than the hangingwall because of the higher confining pressure and inferred paucity of fluids, so that failure should be much less prominent. If Coulomb–Navier fracture does occur, it would be extensional failure. This could not contribute to the shallow relief of compressive mismatch stress but may be a significant cause of relief of mismatch tension near the bottom of the faulted layer. For much larger extension of the layer than in our model, tensile failure may affect the footwall plate near to the fault from top to bottom causing tensile failure of the whole layer which terminates the faulting (Bott, 1997).

These results suggest a major contrast between hangingwall and footwall structure. Further more sophisticated modelling is needed to follow the changing stress environment associated with the earthquake cycle involving successive locking and unlocking of the fault. In the meantime the modelling can be tested by field observation.

8.4. Shallow normal drag in the hangingwall

Normal drag (i.e. convex towards slip direction) used to be attributed to friction on the fault plane (e.g. Billings, 1972), as implied by its name. However, the boundary force distribution which drives normal faulting acts on the fault planes and not within the interior of the plates (Fig. 4), so that friction cannot produce fault drag. Reches and Eidelman (1995) used finite element methods to model a short planar fault pinned to zero displacement at its ends in a deforming elastic or elastoplastic medium. They showed that the flow in the enclosing medium produced a pattern of normal and reverse drag along the fault and concluded that
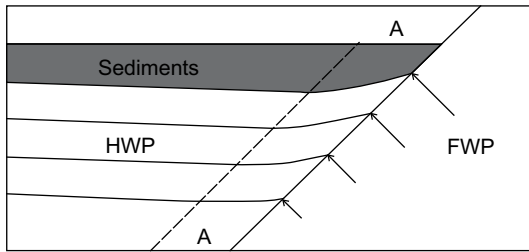
Fig. 12. Sketch, not to scale, to illustrate the mechanism suggested for the origin of the so-called normal 'drag', depending on the downward decreasing compressive traction applied to the upper part of the hangingwall in suppression of mismatch. HWP denotes hangingwall plate, FWP denotes footwall plate, and A–A denotes the fault-parallel zone of weakness adjacent to the hangingwall. Arrows denote the compressive tractions acting perpendicular to the fault plane which produce the 'drag'.

friction does not cause the drag. Similar results were obtained by Grasemann et al. (2005) using elastic analysis. These results, however, fail to explain normal drag on a long planar normal fault unpinned at the ends, such as is modelled here. The only explanation that Reches and Eidelman (1995) could suggest was a shear-zone type of deformation prior to faulting, following Dennis (1972).

The suppression of shallow mismatch provides a new explanation for the so-called normal drag at shallow depths adjacent to the hangingwall of a normal fault (Fig. 12). The potential mismatch of 0.223° affecting the normal fault model (Table 1) requires a horizontal shortening of 35 m at the top of the layer and an equal stretching at the base. This strain is probably mainly relieved at shallow depth by spasmodic fault-perpendicular shortening of the weak zone adjacent to the hangingwall, although some more distant shallow relief may occur along the top of the hangingwall, and in response to bending stresses along the footwall uplift (Fig. 10b and c). The shallow footwall and the adjacent part of the footwall plate cannot contribute to the relief of mismatch shortening strain because of its fault-perpendicular deviatoric tension.

The strain release in the weak zone along the hangingwall may occur by Coulomb–Navier fracture as described in the previous section or by plastic deformation of incompetent strata. Maximum shortening strain should occur adjacent to the fault with the strain progressively decreasing away across the zone of weakness. Fault-perpendicular shortening implies an equal extensional strain upwards along the fault plane since downward extension is blocked. The strain release therefore decreases across the failure zone away from the fault plane and increases upwards towards the top of the hangingwall, simulating the effect of normal drag (Fig. 12).

The simulated normal drag possibly extends over a horizontal distance of a few tens of metres from the hangingwall (Fig. 12). The maximum development must be at the original top of the hangingwall plate with the amplitude decreasing downwards. Sediments which accumulate adjacent to the fault as it develops are also vulnerable to such deformation, with the amplitude of the 'drag' decreasing upwards.

9. Conclusions

1. A simple elastic finite element model of a uniform upper crust of 12 km thickness above an inviscid substratum, cut by a planar normal fault of 1000 m throw dipping at 45°, has been used to explore the stresses associated with normal faulting. In particular, the origin of shallow compressive stress above the hangingwall as seen in earlier modelling has been investigated. The upper crustal density in the model is 2750 kg/m^3 and the half graben is filled by sediments of density 2350 kg/m^3.

Shallow sub-horizontal compression occurs at the top of the hangingwall plate out to about 14 km from the fault trace, peaking at 26 MPa about 5 km from the fault where the tension due to stretching and bending is swamped.

2. The anomalous shallow compression and deep tension are caused by a potential difference in hangingwall and footwall dips which would arise from the differing dips of the plates at the fault if unconstrained to remain in contact. This would cause unrestrained fault planes to diverge downwards. This is prevented by earth pressure which forces the fault planes to remain in contact.

3. This mismatch effect has been studied quantitatively by extracting the equal but opposite nodal forces acting on the fault planes from the deformed elastic model shown in Figs. 2 and 3. On each fault plane, these can be separated into irrotational linear forces and a couple. The equal but opposite irrotational force distributions give rise to the stretching and most of the bending of each plate. The equal but opposite couples ensure that the plates remain in contact along their joint length. This produces shallow compression in *both* plates as they are forced together at the top and deep tension of similar magnitude as they are pulled apart at the bottom.

4. In order to separate the deformation and stresses produced by the irrotational forces from that caused by the couples, these forces and couples have been applied separately to hangingwall and footwall plates in two stages. **Stage 1** applies the deformation and stress field produced by the irrotational linear forces only (Table 1, Fig. 6a). Both plates rotate clockwise, the hangingwall by −0.661° and the footwall by −0.438°, producing a downward widening mismatch of −0.223°. **Stage 2** applies the couples separately to each deformed plate (treated as unstressed) to isolate the mismatch suppression stresses (Table 1, Fig. 6b) producing rotations of +0.121° for the hangingwall and −0.103° for the footwall. This exactly corrects the mismatch, producing a rotation of −0.540° for each plate with nearly exact agreement with the rotation of −0.541° for the fault plane in the original model. The upthrow and downthrow also agree to good precision.

5. The separation of the bending and stretching stress distribution (Fig. 6a) from the mismatch suppression stress distribution (Fig. 6b) isolates these two contributions. The mismatch suppression stresses decrease away from the fault in both directions, dying off to small values at 75 km (footwall) to 100 km (hangingwall) from the fault. They are compressive at shallow depth and tensional near the bottom of the layer. Extrapolated to the surface, they peak at about 32 MPa. They are less prominent than the bending stresses but larger than the stress due to simple stretching.

6. Compressive bending stresses follow round the obtuse angles at the top of the footwall and bottom of the hangingwall and continue parallel to each fault plane along its length (Fig. 6a). Likewise the mismatch suppression stresses also bend round adjacent to these obtuse angles and continue along the length of the fault plane; these are compressive in the footwall plate but tensional in the hangingwall plate (Fig. 6b). The combined effect is strong fault-parallel compression and increased pressure adjacent to the footwall but weaker tension and decreased pressure adjacent to the hangingwall (Fig. 3b).

7. Comparison of the mismatch developed in comparable normal and reverse faults with both equal and differential isostatic loading enables the isolation of two contributions to the potential mismatch, one caused by differential isostatic loading and the other caused by the anti-symmetry of the footwall and hangingwall plates. These two contributions oppose each other

in normal faulting but reinforce in reverse faulting. Consequently, mismatch in the differentially loaded reverse-faulted model is about 3.4 times larger than that in the normal-faulted model.

8. Stress caused by suppression of mismatch occurs in most models of normal (and reverse) faulting. Its magnitude is only moderately influenced by the dip of the fault, the layer thickness, elastoplastic Byerlee-law rheology and friction. The main controlling influence is the density differential between the basement and the half graben infill. In normal faulting, shallow mismatch compression is replaced by tension when the infill has a density of $1000\,kg/m^3$ (water infill) or less, with maximum tension when it is empty.

9. A large and abrupt change in confining pressure and deviatoric stress occurs across the fault plane between hangingwall and footwall (Fig. 11). The hangingwall forms a trough of minimum confining pressure, providing a channel for upward flow of pressurized hydrothermal fluids to the surface. The high fluid pressure at shallow depths and low confining pressure give rise to a zone of minimum strength where the rising fluids may open tension cracks and react with the wall rock to form gouge. The fault-perpendicular deviatoric pressure causes spasmodic Coulomb–Navier fracture and/or incompetent plastic strain to relieve mismatch strain and hence to give rise to the so-called 'normal fault drag'.

10. In contrast, high confining pressure and fault-parallel deviatoric compression dominate along the footwall, giving rise to a belt or maximum strength which inhibits fluid flow, especially across the fault. The ridge-perpendicular deviatoric tension cannot contribute to relief of the shallow mismatch shortening strain but probably provides the main relief of extensional mismatch strain near the bottom of the layer. Non-elastic failure is unlikely to be prominent along or near to the shallow footwall until the throw of the fault is much more than 1000 m.

Acknowledgements

References

Anderson, E.M., 1951. The Dynamics of Faulting, Second ed. Oliver & Boyd, Edinburgh.

Billings, M.P., 1972. Structural Geology, Third ed,. Prentice-Hall, Englewood Cliffs, NJ.

Bott, M.H.P., 1996. Flexure associated with planar faulting. Geophysical Journal International 126, F21–F24.

Bott, M.H.P., 1997. Modeling the formation of a half graben using realistic upper crustal rheology. Journal of Geophysical Research 102B, 24605–24617.

Bott, M.H.P., Kusznir, N.J., 1984. The origin of tectonic stress in the lithosphere. Tectonophysics 105, 1–13.

Dennis, J., 1972. Structural Geology. John Wiley, New York, NY.

Grasemann, B., Martel, S., Passchier, C., 2005. Reverse and normal drag along a fault. Journal of Structural Geology 27, 999–1010.

Gunn, R., 1943. A quantitative evaluation of the influence of the lithosphere on the anomalies of gravity. Journal of the Franklin Institute 236, 47–65.

Jackson, J.A., 1987. Active normal faulting and crustal extension. In: Coward, M.P., Dewey, J.F., Hancock, P.L. (Eds.), Continental Extensional Tectonics. Geological Society, London, Speical Publication, vol. 28, pp. 3–17.

Jackson, J.A., White, N.J., 1989. Normal faulting in the upper continental crust: observations from regions of active extension. Journal of Structural Geology 11, 15–36.

King, G.C.P., Cocco, M., 2001. Fault interaction by elastic stress changes: new clues from earthquake sequences. Advances in Geophysics 44, 1–38.

King, G.C.P., Muir Wood, R., 1994. The impact of earthquakes on fluids in the crust. Annali di Geofisica 37, 1453–1460.

Kusznir, N.J., Marsden, G., Egan, S.S., 1991. A flexural-cantilever simple-shear/pure-shear model of continental lithosphere extension: applications to the Jeanne d'Arc Basin, Grand Banks and Viking Graben, North Sea. In: Roberts, A.M., Yielding, G., Freeman, B. (Eds.), The Geometry of Normal Faults. Geological Society, London, Special Publication, vol. 56, pp. 41–60.

Muir-Wood, R., King, G.C.P., 1993. Hydrological signatures of earthquake strain. Journal of Geophysical Research 98B, 22035–22068.

Reches, Z., Eidelman, A., 1995. Drag along faults. Tectonophysics 247, 145–156.

Roberts, A.M., Yielding, G., 1991. Deformation around basin-margin faults in the North Sea/mid-Norway rift. In: Roberts, A.M., Yielding, G., Freeman, B. (Eds.), The Geometry of Normal Faults. Geological Society, London, Special Publication, vol. 56, pp. 61–78.

Rutter, E.H., Holdsworth, R.E., Knipe, R.J., 2001. The nature and tectonic significance of fault-zone weakening: an introduction. In: Holdsworth, R.E., Strachan, R.A., Magloughlin, J.F., Knipe, R.J. (Eds.), The Nature and Tectonic Significance of Fault Zone Weakening. Geological Society, London, Special Publication, vol. 186, pp. 1–11.

Sibson, R.H., 1983. Continental fault structure and the shallow earthquake source. Journal of the Geological Society, London 140, 741–767.

Sibson, R.H., 1989. Earthquake faulting as a structural process. Journal of Structural Geology 11, 1–14.

Watts, A.B., 2001. Isostasy and Flexure of the Lithosphere. Cambridge University Press.

Yeats, R.S., Sieh, K., Allen, C.R., 1997. The Geology of Earthquakes. Oxford University Press.